Available online at www.sciencedirect.com
SCIENCE DIRECT
Polymer 46 (2005) 12612–12625
polymer
www.elsevier.com/locate/polymer

Modelling of liquid crystalline compound fibres

J.I. Ramos *

Room I-320-D, E.T.S. Ingenieros Industriales, Universidad de Málaga, Plaza El Ejido, s/n, 29013 Málaga, Spain

Received 14 July 2005; received in revised form 31 October 2005; accepted 1 November 2005

Abstract

A model for slender, liquid crystalline, bicomponent fibres at low Reynolds and Biot numbers based on the slenderness ratio as the perturbation parameter, is presented. The model results in one-dimensional equations for the fibre's radii, axial velocity component and temperature, to which we have added two transport equations for the molecular orientation and crystallization and the effects of these variables on the elongational viscosity. The crystallization kinetics is based on Avrami–Kolmogorov theory and is affected by the molecular orientation, while the latter is based on Doi's slender body theory for liquid crystalline polymers. It is shown that the model depends on a large number of dimensionless parameters, and shows that the axial strain rate and the degree of molecular orientation increase as the activation energy of the dynamic viscosity of the core, the heat transfer losses, the thermal conductivity ratio and the pre-exponential factors ratio are increased, whereas they decrease as the thermal capacity of the core is increased. It is also shown that the degree of molecular orientation increases and reaches a value equal to one, whereas no complete crystallization is achieved. It is also shown that the crystallization first increases sharply and then at a smaller pace. It is also shown that the axial stresses on liquid crystalline bicomponent fibres are much higher than those on amorphous ones.

Keywords: Compound fibres; Fibre spinning; Crystallization

1. Introduction

In bicomponent melt-spinning processes, two polymers are co-extruded through a small hole in a plate into ambient air to form a single filament or compound fibre with the desired cross-section. The resulting extrudate is simultaneously extended and wound up on a rapidly rotating drum. Solidification takes place between the plate and the drum, and large extensions rates, rapid cooling, and high speeds are usually involved. This manufacturing process is of great interest due to its commercial applications in the production of, for example, fibres for thermal bonding, electrically conducting fibres, textile fibres, optical fibres, etc., e.g. [1–3].

Since in many applications including textile fibres, optical fibres, reinforced fibres, etc., the sheath material either protects the core, serves as a waveguide in signal transmission or is a more costly material than the core with more desirable surface properties, the combination of two different materials with different properties can result in a composite fibre with desirable global properties.

Although there has been quite a lot research on the development of one-dimensional, mathematical models for the analysis of single-component filaments and jets under both isothermal and non-isothermal conditions at low Reynolds numbers [4–6], bicomponent or compound fibres such as those used in reinforced materials and optical fibres have received very little attention.

Previous studies of bicomponent fibres have mainly considered isothermal flows [7–13]. The most remarkable non-isothermal study of bicomponent fibres known to the author is that of Kikutani et al. [14] who modelled the high-speed melt spinning of bicomponent fibres consisting of poly(ethylene terephthalate) (PET) in the core and polypropelene (PP) in the sheath by means of simple, one-dimensional equations of mass, linear momentum and energy conservation, and included both Newtonian and upper-convected Maxwell rheologies and drag on the fibre.

All previous modelling studies of bicomponent fibres have dealt with amorphous materials. However, it is well known that properties of plastic products manufactured by heating the polymer to above its melting temperature and then deforming the melt while simultaneously cooling it to get the desired shape as in melt spinning, depend on the processing conditions to which the polymer is subject during its manufacture. Furthermore, depending on the molecular structure and processing conditions, the final product can be in either an

* Tel.: +34 95 2131402; fax: +34 95 2132816.
E-mail address: jirs@lcc.uma.es.

0032-3861/$ - see front matter © 2005 Elsevier Ltd. All rights reserved.
doi:10.1016/j.polymer.2005.11.008

amorphous or semi-crystalline state. Polymers that are unable to crystallize on cooling below their glass transition temperature, form amorphous solids, and, if these solids are formed by deforming the polymer while cooling it through the glass transition temperature, they can exhibit strong anisotropy. As the deformed amorphous polymer melt cools below its glass transition temperature, its molecules lose their mobility and become frozen in their oriented configuration.

The phase change from the amorphous to the semi-crystalline stage is referred to as a phase transition. Early work on phase transitions considered that heat conduction was dominant and assumed that the temperature was the basic variable. Mean-phase field models were subsequently developed; these models introduce both the temperature and an order parameter, modify the energy equation to account for the order parameter, and introduce an additional equation the origin of which can be traced back to the Landau–Ginzburg theory of phase transitions. However, in most situations of practical interest, other mechanisms than conduction, e.g. deformation of the solid, take place and must be considered by introducing the kinematics of both the liquid and solid.

In the liquid phase, there are density fluctuations caused by thermal agitation [15,16]. These fluctuations may eventually create small clusters or aggregates of polymer molecules having the same properties as the crystalline phase; the small crystals are continuously being created and destroyed by fluctuations because the formation of a crystal involves the creation of an interface between the liquid and the crystal and its consequent energy cost. Moreover, surface effects are dominant in clusters of small size and, as a consequence, their growth is not energetically favorable, and the small crystals tend to dissolve. There exists, however, a critical size beyond which volume effects dominate over surface ones, and the growth of the cluster is favored by a global reduction of energy. The size that determines the stability of the clusters is called critical size, and the process of formation of crystals of size larger than or equal to the critical size is called nucleation. There are two basic types of nucleation: homogeneous nucleation which occurs in the bulk of a pure substance and heterogeneous nucleation which takes place in the presence of impurities, pre-existing crystals, boundaries, etc.

Nucleation is the first step in the crystallization process, for it determines the appearance of the first crystal nuclei which are the germ of the second stage of crystallization, i.e. growth. In this second stage, nuclei larger than the critical size tend to grow either through the addition of monomers or by acting as sites of heterogeneous nucleation, e.g. nucleation on the surface of a growing crystal.

Nucleation is an activated process where an energy barrier has to be overcome in order to form nuclei of a critical size, beyond which the new phase grows spontaneously. Flow-induced crystallization in melts has been modelled in a number of different manners. A frequently used approach is based on the Avrami–Kolmogorov equation [17–20]. This equation was initially developed for isothermal, quiescent crystallization, although it has been extended to account for non-isothermal conditions [21–24] and enhanced crystallization due to the flow. In this approach the effect of the flow is accounted for by the inclusion of an orientation factor which depends on the flow [5]. Another approach is based on an extension of the work of Flory [25] on the stress-induced crystallization of rubber. Such an extension assumes that the temporary network junctions play the same role as the chemical cross-links in the theory of rubber crystallization. A third approach is based on the formulation of constitutive equations that involve the concept of multiple natural configurations and obtain evolution equations for the natural configuration and mass fraction of the crystalline material by maximizing a prescribed rate of dissipation [26].

It is commonly accepted that crystallization kinetics is triggered by a combination of orientation, stress and temperature conditions [5], and it is well known that non-isothermal effects due to the rapid cooling by the surrounding quench air and the low thermal conductivity of fibres can result in non-uniform fibre microstructure and (mechanical, electrical, chemical, optical) properties. As a result, skin-core differentiation or molecular orientation and structure can be observed in many fibres. Although considerable efforts have been made to understand the dynamics of the melting spinning process and the relationship between spinning conditions and fibre structure, most previous studies on melting spinning processes are based primarily on one-dimensional models for single-component round fibres [27–29].

In this paper, we present a one-dimensional model of liquid crystalline bicomponent fibres that accounts for the molecular orientation and crystallization, and uses a Newtonian rheology for both the core and the sheath that depends in an Arrhenius fashion on the temperature. The model is based on an asymptotic expansion of the mass, linear momentum and energy equations for slender axisymmetric fibres to which the effects of crystallization and orientation are added through the solution of two equations for the degrees of molecular orientation and crystallization and their effects on the dynamic viscosity. Since the derivation of the leading-order equations for the bicomponent fibre's geometry, linear momentum and energy follows similar steps to the ones employed by the author in his studies of isothermal, bicomponent fibres [13], only brief comments on its derivation will be made.

The paper has been arranged as follows. In the next section, a brief summary of the one-dimensional equations employed in this study is presented. In Section 3, some sample results illustrating the effects of some parameters on the spinning of liquid crystalline bicomponent fibres are presented. A summary of the main findings of the paper is presented in the last section of the paper.

2. Formulation

The model for liquid crystalline, bicomponent melt-spun fibres presented here is derived from an asymptotic analysis based on the slenderness ratio for amorphous fibres to which we have added the effects of molecular orientation and crystallization. The orientation model is based on Doi's slender body theory of liquid crystalline polymers, while the

crystallization kinetics is based on Avrami–Kolmogorov's theory [17–20] with Ziabicki's theory [5] for the coupling between the crystallinity and the polymer orientation, and Kikutani's empirical law [30] is employed to relate the elongational viscosity of the melt to the degree of crystallinity. A brief description of both submodels is presented in the next two subsections.

2.1. Model for amorphous fibres

Consider an axisymmetric, bicomponent or compound liquid jet such as the one shown schematically in Fig. 1, consisting of two immiscible, incompressible (constant density) fluids which are assumed to be Newtonian. The inner (subscript 1) and outer (subscript 2) jets correspond to $0 \le r \le R_1(t,x)$ and $R_1(t,x) \le r \le R_2(t,x)$, respectively, where t is time, x and r are the axial and radial coordinates, respectively, and R_1 and R_2 denote the inner jet's radius and the outer jet's outer radius, respectively.

The fluid dynamics of the compound jet or fibre are governed by the two-dimensional conservation equations of mass, linear momentum in the radial and axial directions, and energy, plus appropriate boundary conditions at the nozzle exit ($x=0$), downstream or take-up location ($x=L$), initial conditions, symmetry boundary conditions at $r=0$, and kinematic, dynamic and thermal boundary conditions at $R_1(t, x)$ and $R_2(t,x)$. The kinematic conditions indicate that the interfaces at R_1 and R_2 are material surfaces where the velocity field is continuous, whereas the dynamic ones establish the continuity of shear stresses and the balance of the jump in normal stresses by surface tension. In addition, the thermal boundary conditions at the interfaces establish the continuity of the temperature and heat fluxes.

In the model presented here, we assume that the density, ρ_i, specific heat, C_i, thermal conductivity, K_i, and surface tension, σ_i, where $i=1,2$ denote the core and the sheath, respectively, are constant, and the gases surrounding the sheath are dynamically passive. The latter assumption can be justified due to the small density and dynamic viscosity of gases compared with those of liquids. In addition, it is assumed that the dynamic viscosity of the two components of the fibre depends in an Arrhenius fashion on the temperature, T, as

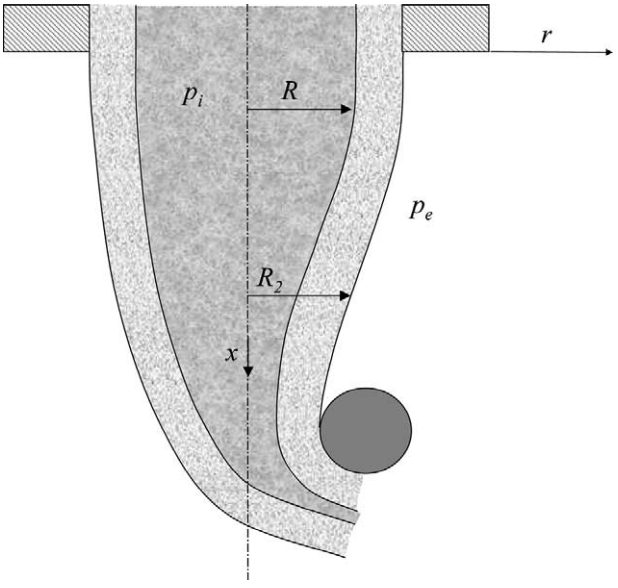

Fig. 1. Schematic of a compound fibre.

$$\mu_i = A_i \exp\left(-\frac{E_i}{T_i - (T_m)_i}\right), \tag{1}$$

where A, E and T_m denote the pre-exponential factor, activation energy and melting temperature, respectively. This equation can be linearized and written as

$$\mu_i = D_i \exp(-H_i(T_i - (T_m)_i)), \tag{2}$$

which indicates that the dynamic viscosity increases exponentially with the temperature for $T < T_m$, and the values of D and H can be easily deduced from Eq. (1).

For slender compound jets at low Reynolds number, i.e. $\varepsilon = (R_0/L) \ll 1$, where R_0 denotes a characteristic radius at the die's exit and L is the distance between the die's exit and the take-up point, it is convenient to nondimensionalize r, x, t, the axial and radial velocity components, u, v, respectively, the pressure, p, density, ρ, specific heat and thermal conductivity, and T with respect to R_0, L, L/u_0, u_0, v_0, $\mu_0 u_0/L$, ρ_0, C_0, K_0 and T_0, respectively, where u_0 is a characteristic (constant) axial velocity component, $v_0 = R_0 u_0/L$, T_0 is a reference temperature, and ρ_0, C_0, K_0 and μ_0 are (constant) reference values for the density, specific heat, thermal conductivity and dynamic viscosity, respectively. Furthermore, for small Reynolds numbers, i.e. $\mathrm{Re} \equiv \rho_0 u_0 R_0/\mu_0 = \varepsilon \bar{R}$, large Froude numbers, i.e. $Fr \equiv (u_0^2/gR_0) = (\bar{F}/\varepsilon)$, large capillary numbers, i.e. $Ca \equiv (\mu_0 u_0/\sigma_2) = (\bar{C}/\varepsilon)$, and small Biot numbers, i.e. $Bi \equiv (hR_0/K_0) = \varepsilon^2 \bar{B}$, where g is the gravitational acceleration, σ_2 is the surface tension at the sheath's outer interface, and h is the film heat transfer coefficient that includes the effects of both convection and radiation, and $\bar{R}$, $\bar{F}$, $\bar{C}$ and $\bar{B}$ are $O(1)$, it is an easy exercise to show that the governing equations and boundary conditions depend on ε^2. Therefore, by expanding the axial and radial velocity components, pressure and temperature as $\phi(t,x,r) = \phi_0(t,x,r) + \varepsilon^2 \phi_2(t,x,r) + O(\varepsilon^4)$, and the fibre's radii as $\psi(t,x) = \psi_0(t,x) + \varepsilon^2 \psi_2(t,x) + O(\varepsilon^4)$ together with the expansion of the boundary conditions about $\psi_0(t,x)$, where ϕ denotes u, v, p and T, and ψ denotes R_1 and R_2, one obtains a sequence of equations that, at leading order, i.e. ε^0, yield that the leading-order axial velocity component and temperature of both the core and the sheath are identical, and the radial velocity component depends linearly on r. In addition, one can easily obtain, by proceeding to $O(\varepsilon^2)$, the following dimensionless one-dimensional equations

$$\frac{\partial A_1}{\partial t} + \frac{\partial (A_1 B)}{\partial x} = 0, \tag{3}$$

$$\frac{\partial A_2}{\partial t} + \frac{\partial (A_2 B)}{\partial x} = 0, \tag{4}$$

$$\bar{R}(\rho_2 A_2+\rho_1 A_1)\left(\frac{\partial B}{\partial t}+B\frac{\partial B}{\partial x}\right)=\bar{R}\bar{F}(\rho_1 A_1+\rho_2 A_2)+\frac{\partial}{\partial x}\left(3(\mu_1 A_1+\mu_2 A_2)\frac{\partial B}{\partial x}\right)+\frac{1}{2\bar{C}}\left(\frac{\partial R_2}{\partial x}+\frac{\sigma_1}{\sigma_2}\frac{\partial R_1}{\partial x}\right), \tag{5}$$

$$\bar{P}(\rho_2 A_2+\rho_1 A_1)\left(\frac{\partial F}{\partial t}+B\frac{\partial F}{\partial x}\right)=\frac{\partial}{\partial x}\left((K_1 A_1+K_2 A_2)\frac{\partial F}{\partial x}\right)+3(\mu_1 A_1+\mu_2 A_2)Br\left(\frac{\partial B}{\partial x}\right)^2-\bar{B}R_2(F-F_\infty), \tag{6}$$

where

$$A_1=\frac{R_1^2}{2},\ A_2=\frac{R_2^2-R_1^2}{2}. \tag{7}$$

and, for conciseness, we have omitted the subscript 0 in the dependent variables, B and F denote the (non-dimensional) leading-order axial velocity component and temperature, respectively, $Br=\mathrm{Pr}(u_0^2/(C_0T_0))$ and $Pr=((\mu_0C_0)/K_0)$ are the Brinkman and Prandtl numbers, respectively, σ_1 is the surface tension at the core-sheath interface, $\bar{P}=Pr\bar{R}$ is the Péclet number, and F_∞ is the non-dimensional temperature of the gases surrounding the cladding.

The condition that the leading order temperatures of the core and cladding are identical allow us to write the leading-order dynamic viscosities as (cf. Eq. (2))

$$\mu_i=G_i\exp(E_i(1-F)), \tag{8}$$

and places some limitations in the applicability of the model presented here, as discussed below.

It must be pointed out that the slender flow approximation employed here is not valid near the die's exit where the flow undergoes a change form no-slip to free-surface conditions, and, therefore, the axial coordinate x is measured not from the die's exit as mentioned above; however, we will continue using this terminology hereon. It must also be pointed out that perfect bonding of the core and sheath has been assumed at R_1 and, as a consequence, there is continuity of the tangential and normal velocity components at R_1.

Note that Eqs. (3)–(6) have been dimensionalized with respect to the (dimensional) reference variables ρ_0, μ_0, C_0 and K_0 which can be set to the corresponding ones for either the core or the sheath. We have, however, preferred to introduce the subscript 0 reference variables in order to clearly illustrate the effects of thermal inertia and thermal conductivity in the one-dimensional equations.

The leading-order equations for the pressure yield

$$p_1=p_e-\mu_1\frac{\partial B}{\partial x}+\frac{1}{\bar{C}}\left(\frac{\partial R_2}{\partial x}+\frac{\sigma_1}{\sigma_2}\frac{\partial R_1}{\partial x}\right), \tag{9}$$

$$p_2=p_e-\mu_2\frac{\partial B}{\partial x}+\frac{1}{\bar{C}}\frac{\partial R_2}{\partial x}, \tag{10}$$

where p_e denotes the pressure of the gases surrounding the cladding and may be set to zero without loss of generality.

2.2. Orientation and crystallization of compound fibres

The molecular orientation and crystallization of compound fibres have been introduced in Eqs. (3)–(9) through a generalization of the model developed by Forest et al. [27] for liquid polymer round fibres. Such a generalization requires the solution of Eqs. (2)–(8) where μ_i is to be replaced by an effective dynamic viscosity, $\mu_{e,i}$, given by

$$\mu_{e,1}=\mu_{10}(F)\exp\left(\beta_1\left(\frac{\theta_1}{\theta_{\infty,1}}\right)^{n_1}\right)+\frac{2}{3}\alpha_1\lambda_1 s_1^2, \tag{11}$$

$$\mu_{e,2}=\mu_{20}(F)\exp\left(\beta_2\left(\frac{\theta_2}{\theta_{\infty,2}}\right)^{n_2}\right)+\frac{2}{3}\alpha_2\lambda_2 s_2^2, \tag{12}$$

in those equations as well as in Eqs. (9) and (10), together with the solution of the following (nondimensional) equations for the degree of orientation, s, defined as the ensemble average of the alignment of the molecular direction to the axial direction, and the degree of crystallinity, θ, of the core and sheath

$$\frac{\partial s_i}{\partial t}+B\frac{\partial s_i}{\partial x}=(1-s_i)(2s_i+1)\frac{\partial B}{\partial x}-\frac{\psi_i}{\lambda_i}U_i(s_i),\quad i=1,2, \tag{13}$$

$$\frac{\partial \theta_i}{\partial t}+B\frac{\partial \theta_i}{\partial x}=k_{\mathrm{A}i}(s)(\theta_{\infty,i}-\theta_i),\quad i=1,2, \tag{14}$$

where $k_{\mathrm{A}i}(s)=k_{\mathrm{A}i}(0)\exp(a_{2i}s_i^2)$ is the linearized growth rate, $k_{\mathrm{A}i}(0)$ is the amorphous growth rate [5], a_{2i} is a constant, $\theta_{\infty,i}$ is the ultimate degree of crystallinity,

$$U_i(s_i)=s_i\left(1-\frac{N_i}{3}(1-s_i)(2s_i+1)\right),\quad i=1,2, \tag{15}$$

is a bulk free energy which is related to the intermolecular potential, ψ is an anisotropic drag parameter ($0<\psi\leq 1$, $\psi=1$ for isotropic models, and $\psi\approx 0.5$ for rigid-rod molecular models), λ is the molecular relaxation time of the liquid crystalline polymer, N is the dimensionless density of the liquid crystalline polymer, α is a parameter that relates the kinetic energy to the inertial energy of the liquid crystalline polymer, β_i is the crystallization viscosity rate and n_i is the crystallization viscosity index.

It must be noted that the effective dynamic viscosity, $\mu_{e,i}$, of Eqs. (11) and (12) contains the effects of temperature through Eq. (8). The effects of crystallization have been assumed to be multiplicative, whereas those of orientation have been assumed to be additive in Eqs. (11) and (12). It must also be noted that μ_i, β_i and n_i are material-dependent, e.g. $\beta_i=4.605$ and $n_i=12$ for nylon-66, $\beta_i=4$ and $n_i=2$ for PET, and that Eqs. (3)–(6), (13) and (14) reduce to those for single-component liquid crystalline filaments [27] when $\rho_1=\rho_2$, $C_1=C_2$, $K_1=K_2$, $\mu_1=\mu_2$ and $\sigma_1=0$, $\psi_1=\psi_2$, $\lambda_1=\lambda_2$, $k_{\mathrm{A}1}(0)=k_{\mathrm{A}2}(0)$, $a_{21}=a_{22}$, $N_1=N_2$, $n_1=n_2$, $\beta_1=\beta_2$, $\theta_{\infty 1}=\theta_{\infty 2}$.

Eq. (13) indicates that the molecular orientation is affected by the axial velocity component, B, and affects the degree of crystallization through Eq. (14); both the orientation and crystallization affect the axial velocity component (Eq. (5)) through the effective dynamic viscosities (Eqs. (11) and (12)),

and, of course, the compound fibre's geometry (Eqs. (3) and (4)) and temperature (Eq. (6)) are affected by the axial velocity component. This implies that the orientation and crystallization of the compound fibre are nonlinearly coupled with the fibre's geometry, axial velocity component and temperature, and that Eqs. (3)–(6), (13) and (14) must be solved numerically in an iterative fashion. However, if $\psi_i = 0$ in Eq. (13), then the resulting equation under steady state conditions can be written as $(ds/dy) = (1-s)(1+2s)$, where $y = \ln B$ and the subscript i has been dropped, and has fixed points at $s = 1$ and $s = -(1/2)$ which are stable and unstable, respectively, and, since $s \geq 0$, it can be easily shown that the solution to this equation evolves towards $s = 1$. Moreover, Eq. (13) with $\psi = 0$ can be integrated analytically subject to, say, $s(0) = 0$, to yield the molecular orientation as a function of the leading-order axial velocity component as

$$B(x) = \frac{(1+2s)^2}{1-s}, \tag{16}$$

which is a quadratic expression from which one can easily obtain $s(B)$. Furthermore, under the same assumptions as discussed above, Eq. (14) can be integrated analytically subject to $\theta(0) = 0$ to yield

$$\frac{\theta_\infty}{\theta - \theta_\infty} = \int_0^x \frac{k_A(s)}{B(x)} dx, \tag{17}$$

where $k_A(s) = k_A(0)\exp(a_2 s^2)$ can be written as $k_A(B)$ upon using $s(B)$ from Eq. (16). Both Eqs. (16) and (17) indicate that, under the above assumptions, the molecular orientation and crystallization depend on $B(x)$ which, in turn, depends in a nonlinear fashion on the solutions to Eqs. (3)–(6) with μ_i replaced by $\mu_{e,i}$.

As stated above, the one-dimensional Eqs. (3)–(6), (13) and (14) place some limitations on the applicability of the model presented here, for this one-dimensional model does not provide any information about radial variations, especially, those of temperature, and on the implications of these variations on the fibre microstructure. Moreover, if the model overestimates the heat transfer at the fibre's outer surface, it will predict inaccurate temperature fields which, in turn, influence the average axial velocity, tensile stress, crystallinity, and free-surface shape due to the nonlinear couplings between the mass, linear momentum and energy equations. Through the dependence of the crystallization kinetics on temperature and molecular orientation, a crystallinity profile is developed in the radial direction, and the radial variation of the molecular orientation and crystallinity may have a strong influence on the fibre microstructure and properties, i.e. physical, mechanical, thermal, chemical, electrical and optical properties, such as tensile modulus and optical birefringence. In addition, the radial dependence of the temperature field may be of great importance in bicomponent fibres due to the difference in the thermal conductivities of the core and sheath. Moreover, the model presented above does not account for latent heat effects associated with crystallization/phase changes and the effects of the core-sheath interface on molecular orientation and crystallization.

Although, in this paper we shall be concerned with Eqs. (3)–(6), (13) and (14) under steady conditions, it must be noted that some of the limitations of the one-dimensional model mentioned above can be avoided by employing the one-dimensional equations for the compound fibre's leading-order geometry and axial velocity component presented above, while the temperature, orientation and crystallization fields can be determined from the solution of the appropriate two-dimensional equations. If this is done, one must account for the radial variations of the dynamic viscosity due to the radial dependence of the temperature field and the degrees of orientation and crystallization, so that one has to solve Eqs. (3) and (4) for the fibre's geometry, and Eq. (5) with $\mu_1 = (1/A_1)\int_0^{R_1} \mu_1 r dr$ and $\mu_2 = (1/A_2)\int_{R_1}^{R_2} \mu_2 r dr$ and use the leading-order radial velocity component, $v = -((r/2)(\partial B/\partial x))$, to determine the two-dimensional distributions of temperature, orientation and crystallization in the compound fibre. However, this hybrid one-two-dimensional model may not offer any computational advantage over a full two-dimensional model for the mass, linear momentum and energy conservation equations, and for the degrees of molecular orientation and crystallization.

It must also be noted that latent heat effects associated with the solidification of the fluids for the core and sheath have been disregarded and that the solidification occurs through the exponential increase of the dynamic viscosity when the temperature drops below the melting one (cf. Eqs. (1), (2) and (8)). It must, finally, be noted that Eqs. (3)–(15) are dimensionless and according to the nondimensionalization introduced in this paper $0 \leq x \leq 1$, and that dimensional quantities can be easily recovered by undoing the scaling. This last point must be kept in mind in the next section where the results are presented. Moreover, the Reynolds, Froude, Brinkman, Biot and capillary numbers introduced above are based on dimensional quantities, and the nondimensional Biot number, $\bar{B}$, includes the effects of convection and radiation, although it will be considered as constant in the results presented in the next section.

Even though the one-dimensional equations reported above represent a simplification compared with a full two-dimensional model for liquid crystalline bicomponent fibres, it must be stressed that this model depends on large number of dimensionless parameters, i.e. $R_1(0)$, $R_2(0)$, $B(1)$, N_i, ψ_i, α_i, a_{2i}, λ_i, $\theta_i(0)$, $\theta_{\infty,i}$, $s_i(0)$, n_i, β_i, $\bar{R}$, p_e, $\bar{R}/\bar{F}$, $\bar{C}$, $((\rho_1 C_1)/(\rho_2 C_2))$, K_1/K_2, E_1, E_2, G_1/G_2, σ_1/σ_2, $k_{A1}(0)$, $k_{A2}(0)$, $F(0)$, and F_∞. Since the effects of the fibre's radii at the die's exit, Reynolds, Froude and capillary numbers, density and surface tension ratios, and take-up speed on the dynamics and linear stability of isothermal bicomponent jets have been previously discussed by the author [13], we shall only consider the effects of some of the remaining parameters on nonisothermal, liquid crystalline, compound fibres. Furthermore, since the effects of the Brinkman number, i.e. viscous dissipation, were found to be

small for the parameters considered in the next section, we shall only consider $Br=0$, and, unless otherwise stated, $(K_2/K_1)=(\rho_2/\rho_1)=(C_2/C_1)=(G_2/G_1)=1$ and $\bar{P}=1$. Note that when the compound fibre solidifies, the leading-order axial velocity component becomes constant and viscous dissipation is nil.

Note that Eqs. (3)–(15) have been dimensionalized with respect to the reference variables ρ_0, μ_0, C_0 and K_0 which can be set to the corresponding ones for either the core or the sheath. We have, however, preferred to introduce the subscript 0 reference variables in order to clearly illustrate the effects of thermal inertia and thermal conductivity in the one-dimensional equations.

The nondimensional leading-order axial forces on the inner and outer jets (nondimensionalized with respect to $\varepsilon\pi\mu_0\mu_0R_0$) are

$$f_x^{(1)} \equiv A_1\sigma_x^{(1)} = A_1\left(3\mu_{e,1}\frac{\partial B}{\partial x}-p_e+\frac{1}{\bar{C}}\left(\frac{1}{R_2}+\frac{\sigma_1}{\sigma_2}\frac{1}{R_1}\right)\right), \tag{18}$$

$$f_x^{(2)} \equiv A_2\sigma_x^{(2)} = A_2\left(3\mu_{e,2}\frac{\partial B}{\partial x}-p_e+\frac{1}{\bar{C}R_2}\right), \tag{19}$$

respectively, where $\sigma_x^{(i)}$ denote the axial stresses in the core ($i=1$) and sheath ($i=2$).

3. Results

The steady state equations corresponding to Eqs. (3)–(6), (13) and (14) were solved numerically subject to the following nondimensional boundary conditions

$$R_1(0)=\alpha, \quad R_2(0)=\gamma, \quad B(0)=1, \quad F(0)=1, \tag{20}$$

$$B(1)=\delta, \quad (K_1A_1+K_2A_2)\frac{\partial F}{\partial x}(1)=0, \tag{21}$$

$$s_1(0)=0.5, \quad s_2(0)=0.5, \quad \theta_1(0)=0, \quad \theta_2(0)=0, \tag{22}$$

that fix the compound fibre's radii at the die's exit through α and γ, δ is the take-up speed, the thermal boundary condition at the take-up point corresponds to no heat flux, and the degrees of orientation and crystallization are set equal to zero at the die's exit, for $N_i=4$, $\psi_i=0.5$, $\alpha_i=5$, $a_{21}=10$, $a_{22}=5$, $\lambda_i=1$, $\theta_{\infty,i}=0.8$, $n_i=12$, $\beta_i=4$, $\bar{R}=1$, $p_e=0$, $(\bar{R}/\bar{F})=1$, $\bar{C}=10^{39}$, $(\rho_1/\rho_2)=1$, $(G_1/G_2)=1$, $(\sigma_1/\sigma_2)=1$, $Q_1=Q_2=0.5$, $\delta=100$, $k_{A1}(0)=k_{A2}(0)=0.005$, and $F_\infty=0$, and the values of the parameters shown in Table 1, where Q_1 and Q_2 denote the nondimensional volumetric flow rates for the core and sheath, respectively. These values were selected so that the crystallization rate for the core is higher than for the sheath, whereas the orientation parameters are identical for both the core and the sheath.

The solution of the steady state form of Eqs. (3)–(6), (13) and (14) was obtained numerically by means of an iterative, conservative, finite difference method that discretizes the diffusion terms by means of second-order accurate central differences and employs first-order upwind differences for the advection terms. The number of grid points in the axial direction was varied so as to obtain grid-independent results and was, at least, 4000, which corresponds to a (nondimensional) grid spacing equal to 2.5×10^{-4}. Due to the nonlinear coupling amongst the (unknown) compound fibre's geometry, axial velocity and temperature fields, underrelaxation factors equal to 0.5 were employed for B, s_i, θ_i and F, and convergence was established whenever

$$\sum_{j=1}^{NP}\frac{1}{NP}\left(\left(\psi_j^{k+1}\right)^2-\left(\psi_j^{k}\right)^2\right)\le 10^{-16}, \tag{23}$$

where NP denotes the number of grid points in the axial direction, k is the kth iteration, and ψ represents B, s_i, θ_i and F.

Table 1
Values of the parameters used in the calculations

Case	E_1	E_2	$\bar{P}_1$	$\bar{P}_2$	$\bar{B}$	K_2/K_1	G_2/G_1
1	30	30	5	5	10	1	1
2	20	30	5	5	10	1	1
3	40	30	5	5	10	1	1
4	30	30	1	5	10	1	1
5	30	30	10	5	10	1	1
6	30	30	5	5	5	1	1
7	30	30	5	5	20	1	1
8	30	30	5	5	10	0.1	1
9	30	30	5	5	10	10	1
10	30	30	5	5	10	1	0.1
11	30	30	5	5	10	1	10

The calculations were initialized with the (guessed) geometry and axial velocity component corresponding to the analytical solution of the viscous, isothermal regime [13], whereas the initial guess for the temperature field was obtained from the analytical solution of Eq. (6) in the absence of viscous dissipation and axial heat conduction which yields an exponential temperature distribution that depends on the integral of R_2 whose value was assumed to be that of the isothermal, viscous flow regime.

Fig. 2 illustrates the effects of the activation energy of the dynamic viscosity of the core, i.e. E_1, on the compound fibre's geometry, axial velocity component and temperature for the parameters shown in Table 1. This figure indicates that the viscosity of the core increases dramatically as E_1 is increased; this is due to the exponential dependence of the viscosity on temperature (cf. Eq. (8)). For the three activation energies considered in Fig. 2, the fibre's radii are almost constant for $x\ge0.6$, and both the solidification and the slope of the axial velocity increase as E_1 is increased.

It is worth noting that, for the largest activation energy of Fig. 2, the temperature at the take-up point is slightly higher than that for the lowest activation energy; this is due to the amplification effect of the temperature caused by the activation energy in the dynamic viscosity law. However, the small temperature differences observed in Fig. 2 have a

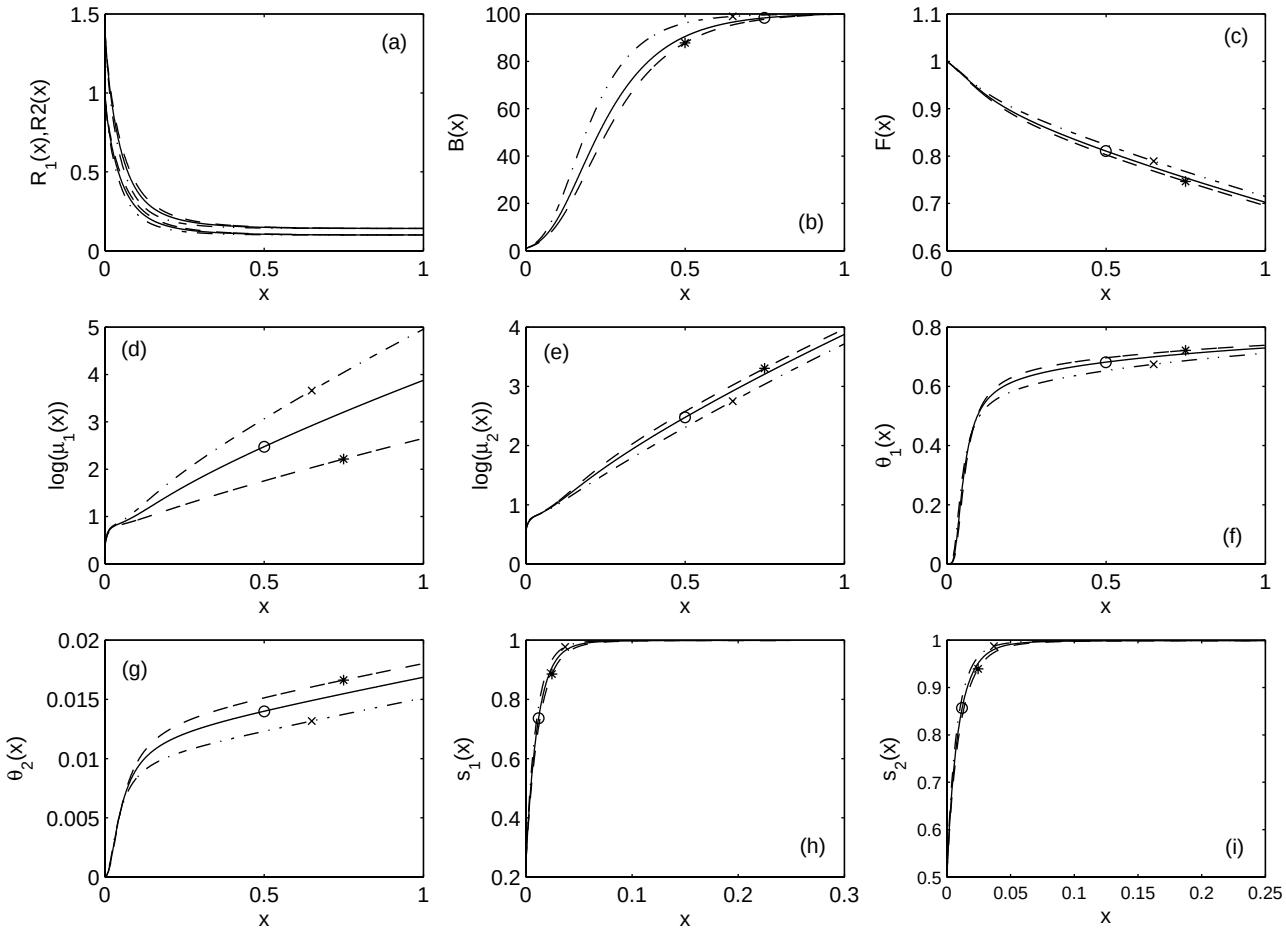

Fig. 2. Compound fibre's geometry (a), axial velocity component (b), temperature (c), dynamic viscosity of the core (d) and sheath (e), degree of crystallization of the core (f) and sheath (g), and degree of molecular orientation of the core (h) and sheath (i). (Solid line and ○: case 1; dashed line and *: case 2; dashed-dotted line and ×: case 3).

large effect on the dynamic viscosity of the core which is larger and increases at a faster rate than that of the sheath for $E_1=40$ and $E_2=30$. For $E_1=E_2$ and values of the other parameters identical to those of Fig. 2, there are small differences between the dynamic viscosities of the core and sheath.

Fig. 2 also shows that the degree of crystallization in the core is higher than that in the sheath, and this result is in accord with the fact that $a_{22}>a_{21}$ in this paper. Both degrees start from a nil value and increase sharply up to approximately $x=0.2$. Beyond this location, the degree of crystallization increases at a lower rate. In any case, for the cases considered in Fig. 2, no complete crystallization, i.e. $\theta_i<\theta_{\infty,i}=0.8$, is achieved before the take-up point. By way of contrast, the degree of orientation increases rapidly to a value of one; in fact, full molecular orientation occurs by about $x=0.1$. The results presented in Fig. 2 also show that the degree of molecular orientation increases as the activation energy of the dynamic viscosity of the core increases, and this is due to the increase in the axial strain rate as E_1 is increased.

Similar results to those shown in Fig. 2 have been found when E_2 was varied, except that the trends of the dynamic viscosity law for the core and sheath are reversed.

Fig. 3 illustrates the axial stresses on the core and sheath, and shows that the axial stresses on the core are monotonic increasing functions of the distance along the fibre for $E_1=30$ and 40, whereas they exhibit a relative maximum at about $x=0.37$ for $E_1=20$. On the other hand, the axial stresses on the sheath are monotonic functions of x for $E_1=30$ and 20, and exhibit a relative maximum at about $x=0.32$ for $E_1=40$. The presence of the relative maximum in the axial stresses on the core is related to the smaller axial velocity gradient and smaller dynamic viscosity for $E_1=20$. As shown in Fig. 2, the axial strain rate and the dynamic viscosity decrease as E_1 is decreased. On the other hand, the relative maximum on the axial stress in the sheath for $E_1=40$ is associated with the activation energy of the dynamic viscosity for the sheath.

The effects of the thermal inertia on the compound fibre have been investigated by varying the thermal Péclet numbers of the core and sheath, i.e. by varying $Pe_i=(\rho_i C_i u_0 R_0/K_i)$ or $(\rho_i C_i)/K_i$ since $\bar{P}_i=\bar{P}((\rho_i C_i)/K_i)$, for $i=1,2$, and some results are presented in Fig. 4. This figure indicates that the drop in temperature along the fibre increases as the Péclet number of the core is decreased, but, for all the activation energies considered in this figure, the axial velocity first increases and then tends to an almost constant value; the slope of the axial velocity profile or axial strain rate increases as the thermal

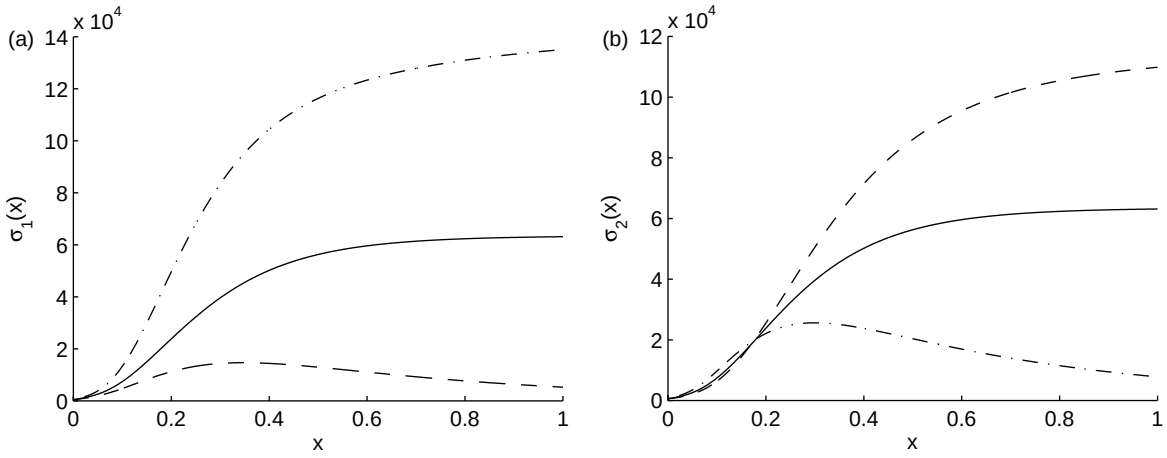

Fig. 3. Axial stress on the core (a) and sheath (b). (Solid line: case 1; dashed line: case 2; dashed-dotted line: case 3).

Péclet number is decreased. This result is to be expected, for an increase in the thermal Péclet number corresponds to an increase in advection, smaller heat transfer losses, and, therefore, a smaller increase in the dynamic viscosity. Similar trends to those presented in Fig. 2 have also been observed when Pe_2 or $\bar{P}_2$ was varied.

Fig. 4 also indicates that the degree of crystallization increases whereas the degree of molecular orientation decreases as the thermal capacity or thermal Péclet number is increased.

Fig. 5 shows that the axial stresses on the core and sheath are monotonic functions of the axial distance along the fibre and increase as the thermal Péclet number is decreased. This is again a

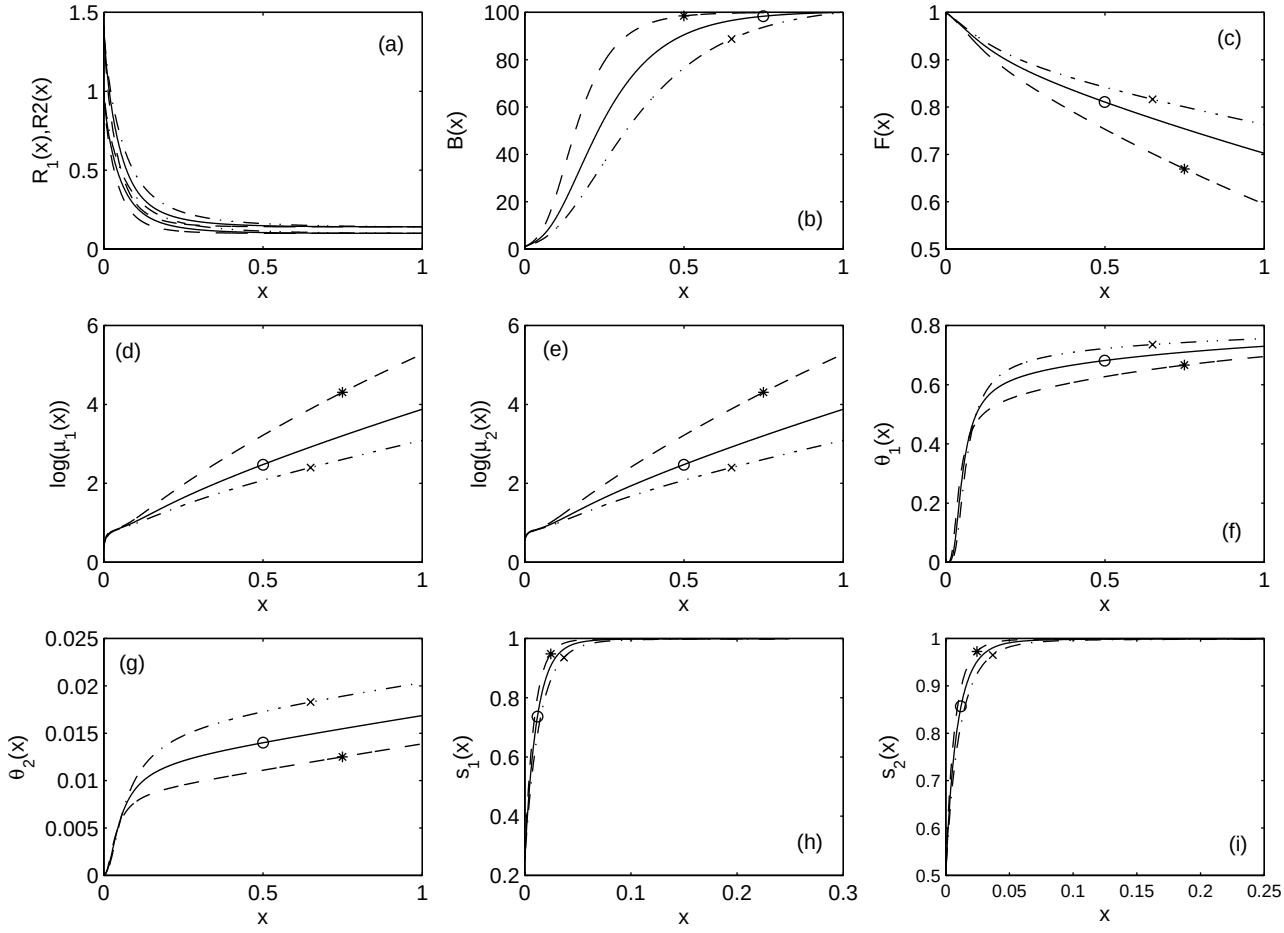

Fig. 4. Compound fibre's geometry (a), axial velocity component (b), temperature (c), dynamic viscosity of the core (d) and sheath (e), degree of crystallization of the core (f) and sheath (g), and degree of molecular orientation of the core (h) and sheath (i). (Solid line and ○: case 1; dashed line and *: case 4; dashed-dotted line and ×: case 5).

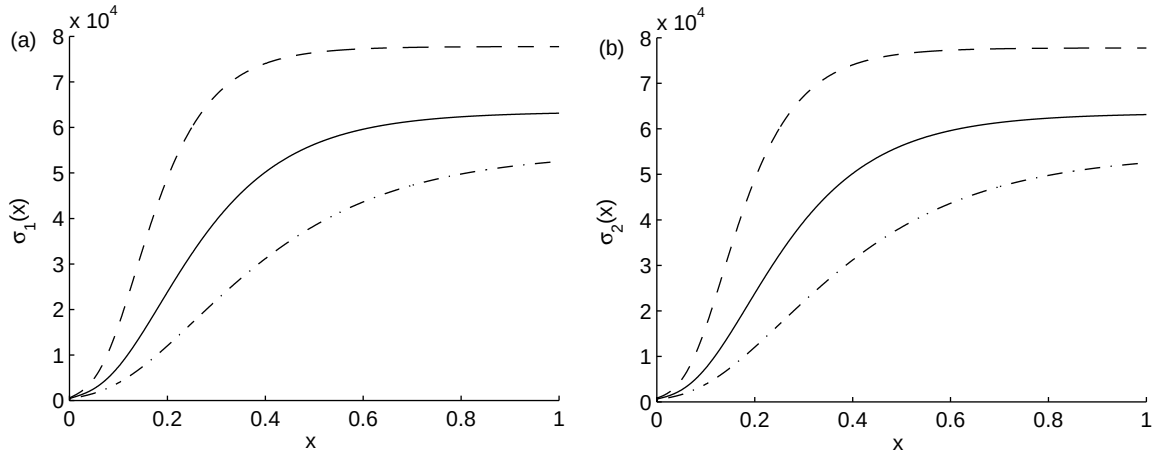

Fig. 5. Axial stress on the core (a) and sheath (b). (Solid line: case 1; dashed line: case 4; dashed-dotted line: case 5).

consequence of the fact that the axial strain rate and dynamic viscosity decrease as the thermal Pécle number is increased.

Fig. 6 illustrates the effects of the Biot number, i.e. $\bar{B}$, or heat losses. For the three Biot numbers of Fig. 6, the axial velocity profile increases and reaches an almost constant value equal to the take-up speed, and the slope of the axial velocity increases as the heat transfer losses increase.

Fig. 6 also shows that the temperature at the take-up point decreases as the Biot number is increased; this decrease, in turn, results in an increase in the dynamic viscosity and fibre's constant radii closer to the die's exit. Moreover, an increase in the heat transfer losses results in a slower degree of crystallization and a faster degree of orientation. For $\bar{B} = 20$, the degree of crystallization is initially steeper than those for

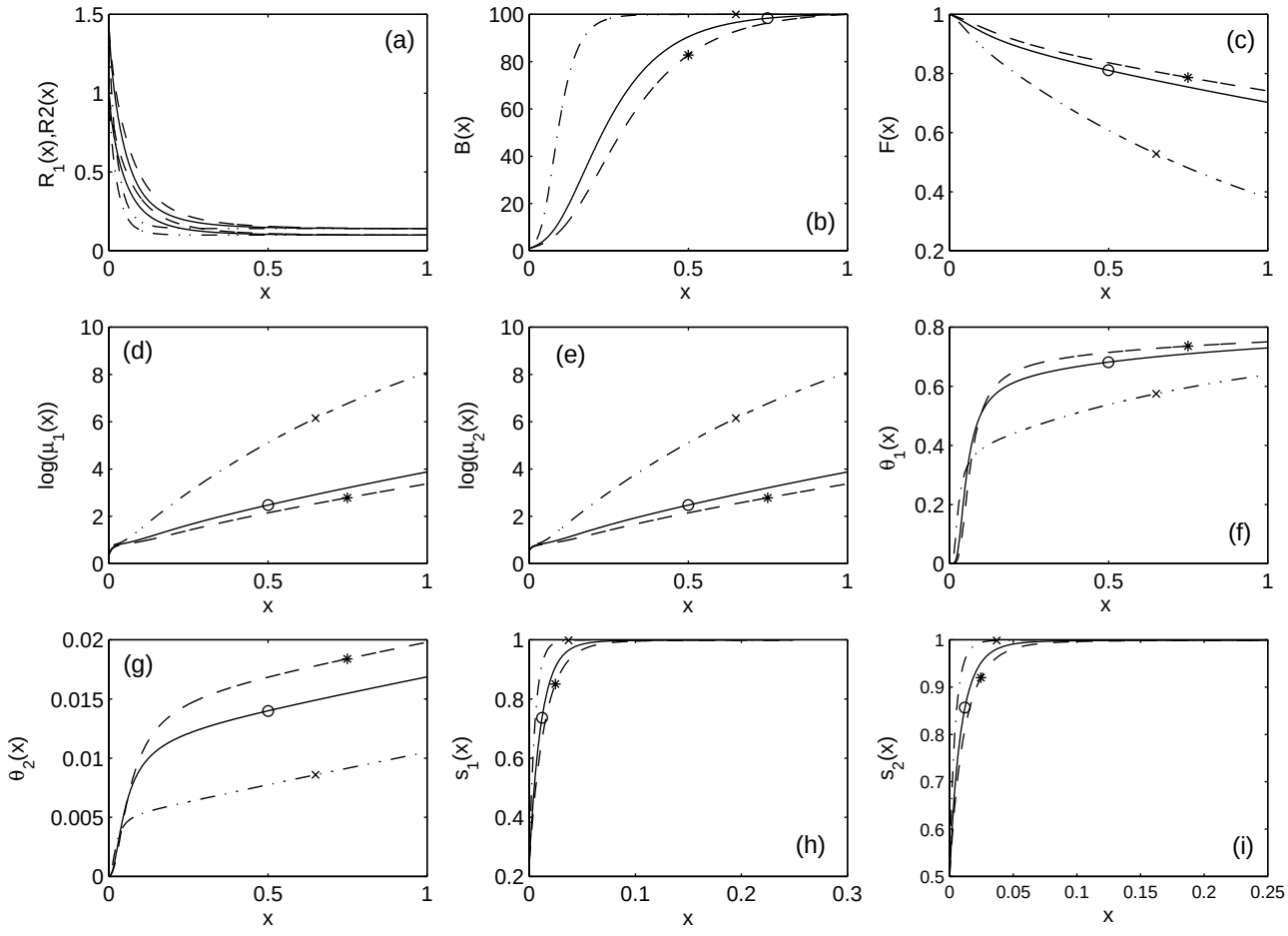

Fig. 6. Compound fibre's geometry (a), axial velocity component (b), temperature (c), dynamic viscosity of the core (d) and sheath (e), degree of crystallization of the core (f) and sheath (g), and degree of molecular orientation of the core (h) and sheath (i). (Solid line and ○: case 1; dashed line and *: case 6; dashed-dotted line and ×: case 7).

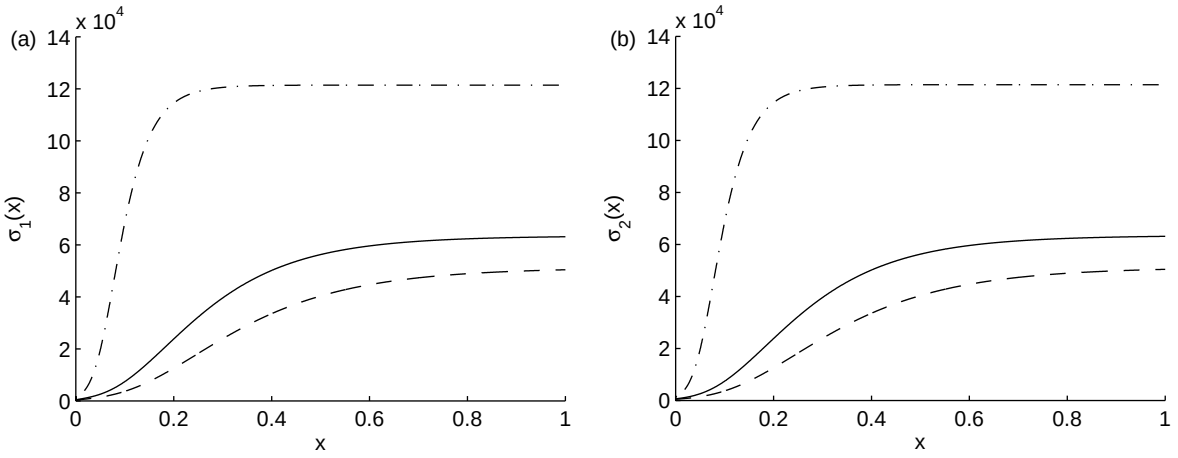

Fig. 7. Axial stress on the core (a) and sheath (b). (Solid line: case 1; dashed line: case 6; dashed-dotted line: case 7).

$\bar{B} = 5$ and 10; however, the degree of crystallization at the take-up point is higher for $\bar{B} = 5$ and 10 than for $\bar{B} = 20$. In addition, although almost full orientation is observed at $x = 0.05$ for $\bar{B} = 20$, only the same is observed at $x = 0.25$ for $\bar{B} = 5$.

The axial stresses on the core and sheath are exhibited in Fig. 7 as functions of the heat transfer losses. As shown in this figure, the axial stresses increase as the Biot number is increased and are monotonic increasing functions of the distance along the compound fibre.

Fig. 8 illustrates the effects of the thermal conductivity ratio, K_2/K_1, on the compound fibre's geometry, axial velocity field and temperature. For the smallest conductivity ratio of Fig. 8,

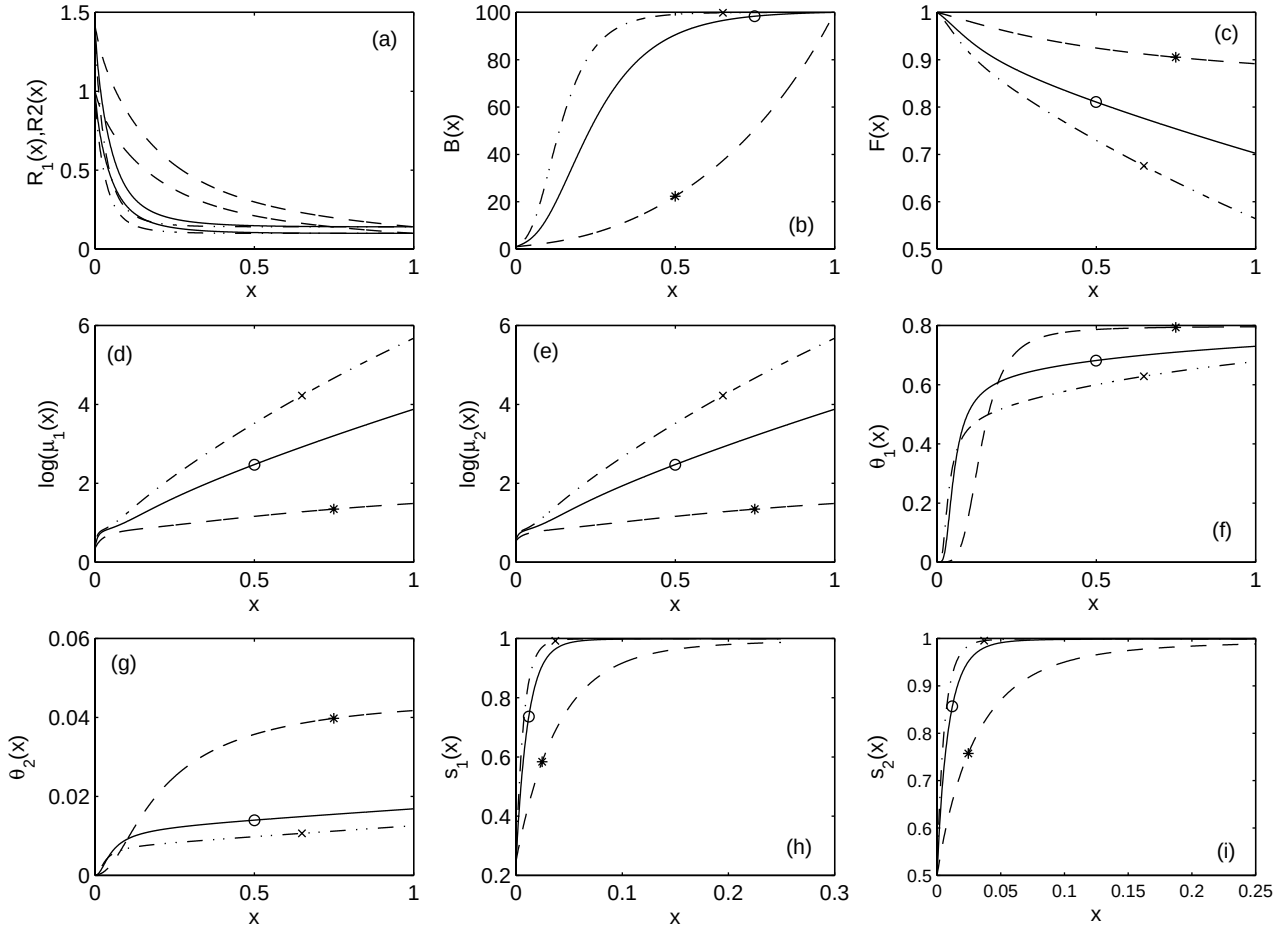

Fig. 8. Compound fibre's geometry (a), axial velocity component (b), temperature (c), dynamic viscosity of the core (d) and sheath (e), degree of crystallization of the core (f) and sheath (g), and degree of molecular orientation of the core (h) and sheath (i). (Solid line and ○: case 1; dashed line and *: case 8; dashed-dotted line and ×: case 9).

the axial velocity profile is concave upwards and increases in an almost exponential manner from the die's exit to the take-up point, whereas the axial velocity increases rapidly for $(K_2/K_1)=1$ and 10. This behavior can be best appreciated in the fibre's geometry, i.e. constant radii are observed for $(K_2/K_1)=1$ and 10, for $x\geq 0.6$, whereas the fibre's radii are not constant for a conductivity ratio equal to 0.1.

Fig. 8 also shows that both the temperature drop and the dynamic viscosity increase as the thermal conductivity ratio is increased. Most remarkable is the fact that compound fibres with low thermal conductivity ratios take a longer distance to start the crystallization process than fibres of higher conductivity. On the other hand, owing to the smaller temperature drop, fibres with low conductivity ratios achieve higher degrees of crystallization at the take-up point than fibres of higher ratios.

Fig. 8 also illustrates that compound fibres of high conductivity ratios have a larger degree of orientation than fibres of smaller ones. In fact, full orientation is observed for $x\geq 0.1$ for $(K_2/K_1)=1$ and 10, whereas no full orientation is observed at the take-up point for $(K_2/K_1)=0.1$. This indicates that the rate of orientation increases whereas the degree of molecular orientation decreases as the thermal conductivity ratio is increased. It must be noted that the axial strain rate increases as the thermal conductivity ratio is increased.

Fig. 9 indicates that the axial stresses are monotonic increasing functions of both the thermal conductivity ratio and the distance along the bicomponent fibre. However, the axial stresses increase sharply initially and then tend to almost constant values for $(K_2/K_1)=1$ and 10, whereas they keep on increasing with x for $(K_2/K_1)=0.1$. These results are in accord with those illustrated in Fig. 8, which indicate that the strain rate and dynamic viscosity increase as the thermal conductivity ratio is increased.

Fig. 10 shows the effect of the ratio of the pre-exponential factors of the dynamic viscosity, and shows that slightly steeper axial velocity profiles are achieved as the pre-exponential factor ratio is increased. Also, the temperature drop and the degrees of orientation and crystallization are not very sensitive functions of this ratio, although the dynamic viscosity of the sheath increases sharply as the pre-exponential factors ratio is increased.

The axial stresses presented in Fig. 11 are monotonically increasing functions of the axial distance along the fibre; those in the core increase whereas those in the sheath decrease as G_2/G_1 is decreased. This result is expected, for an increase in the pre-exponential factors ratio results in an increase of the dynamic viscosity law of the sheath.

Although not shown here, it was found that the degree of crystallization is a strong function of a_{2i} and $k_{Ai}(0)$ (cf. Eq. (14)) but the effects of the degree of crystallization on the dynamic viscosity law (Eqs. (11) and (12)) are much smaller than those associated with the pre-exponential factor and activation energy of the dynamic viscosity law. i.e. Eq. (8). The effects of molecular orientation on the effective dynamic viscosity, i.e. Eqs. (11) and (12), were found to be smaller than those due to the temperature and crystallization.

The results illustrated in this paper and others not shown here indicate that, despite the simplicity and limitations of the one-dimensional model for liquid crystalline bicomponent fibres presented here, a large theoretical and experimental effort must be made to obtain accurate values for the large number of parameters that affect the solidification of bicomponent fibres, especially those related with the dynamic viscosity and the crystallization kinetics.

Table 2 shows the axial stresses on the core and sheath at the die's exit and take-up point, and indicates that the stress at the die's exit and that on the core at the take-up point increase whereas that on the sheath at the take-up point decreases, as the activation energy of the dynamic viscosity of the core is increased. However, as shown in Fig. 3, the axial stresses may exhibit relative maxima. The location of these maxima is equal to 0.3475 and 0.2995 for cases 2 and 3, respectively, and the (nondimensional) stresses in the core at these locations are 1469 and 83,292, respectively, whereas those on the sheath are 61,244 and 25,611, respectively.

Table 2 also shows that the axial stresses on both the core and the sheath at the die's exit and at the take-up point are monotonically decreasing and increasing, respectively, functions of the thermal Péclet and Biot numbers, respectively.

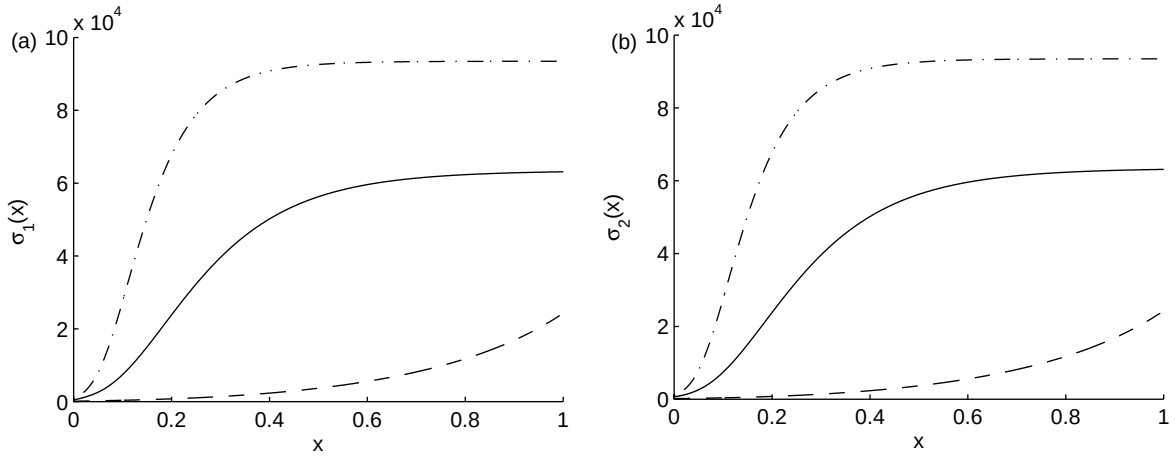

Fig. 9. Axial stress on the core (a) and sheath (b). (Solid line: case 1; dashed line: case 8; dashed-dotted line: case 9).

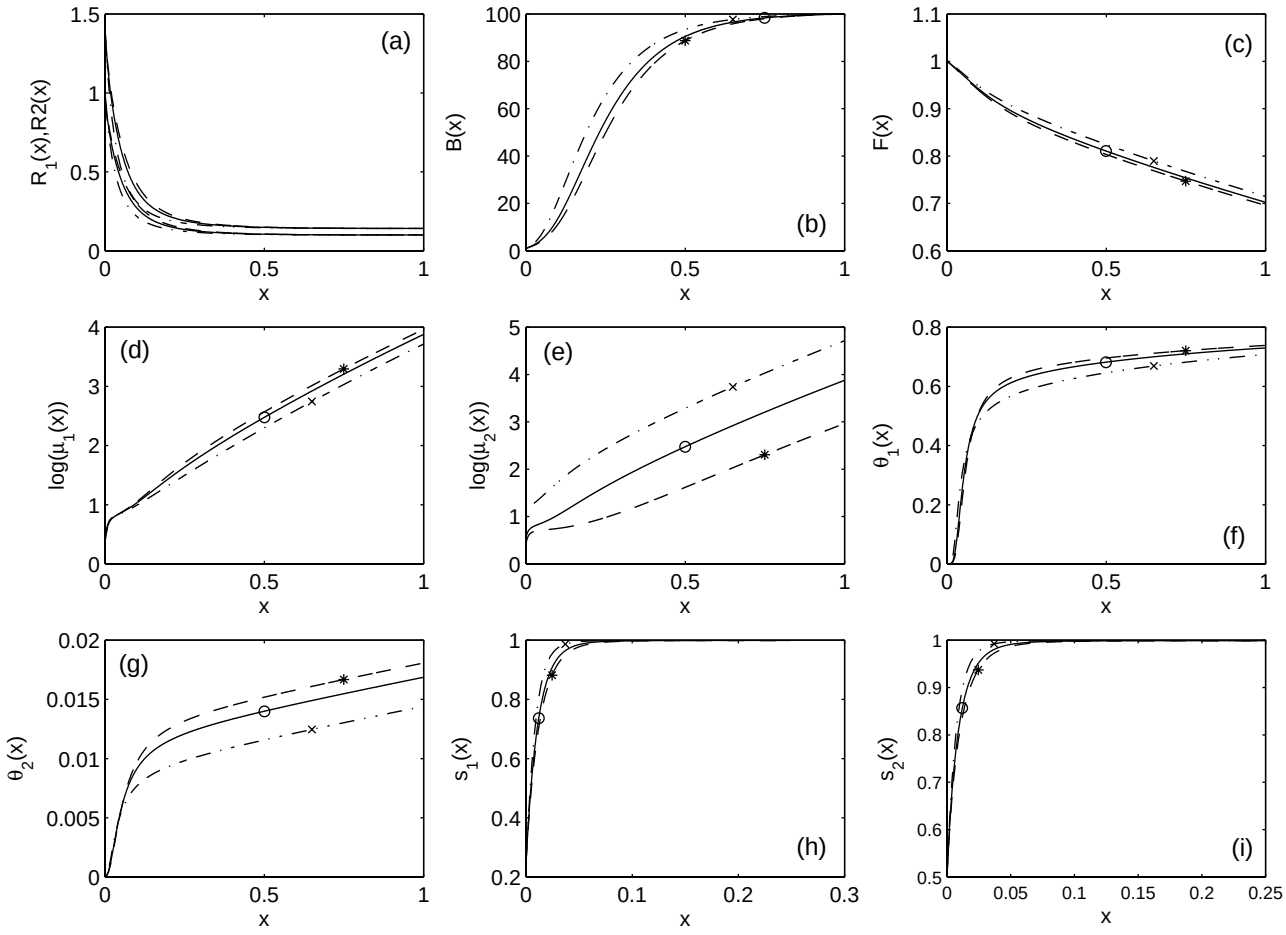

Fig. 10. Compound fibre's geometry (a), axial velocity component (b), temperature (c), dynamic viscosity of the core (d) and sheath (e), degree of crystallization of the core (f) and sheath (g), and degree of molecular orientation of the core (h) and sheath (i). (Solid line and ○: case 1; dashed line and *: case 10; dashed-dotted line and ×: case 11).

These stresses are also monotonically increasing functions of the thermal conductivity ratio.

On the other hand, the axial stresses on the core and sheath at the die's exit and that on the sheath at the take-up point are monotonically increasing functions of the pre-exponential factors ratio, whereas that on the core at the take-up point is a monotonically decreasing function of this ratio. Table 2 also shows that the core-sheath axial stress ratio is almost equal to the pre-exponential factors ratio for cases 9–11.

Calculations have also been performed for amorphous, bicomponent fibres which are governed by Eqs. (3)–(6) with Eq. (8), in order to assess the effects of the molecular orientation and crystallization on the axial stresses on the core and sheath, and, in Table 3, the axial stresses on amorphous

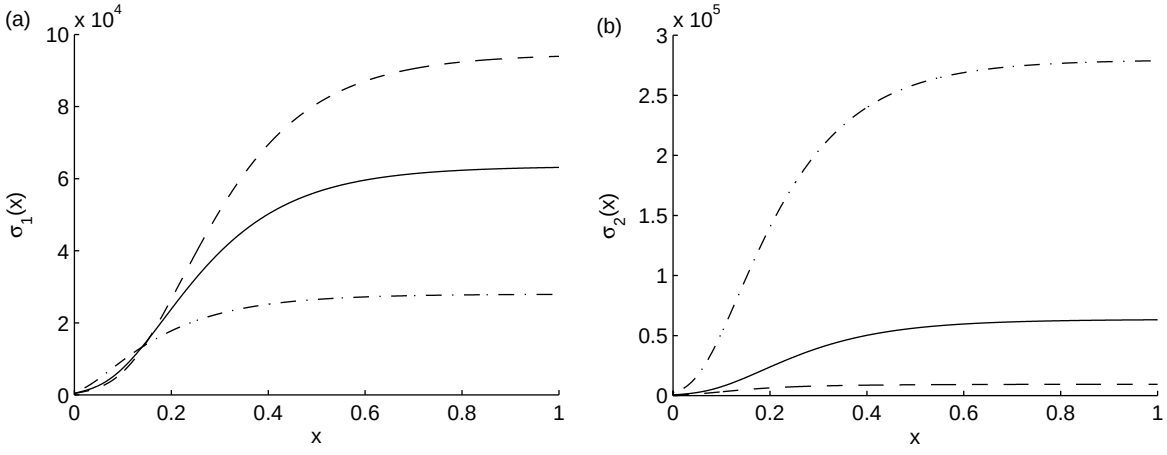

Fig. 11. Axial stress on the core (a) and sheath (b). (Solid line: case 1; dashed line: case 10; dashed-dotted line: case 11).

Table 2
Nondimensional axial stresses on the core and the sheath for liquid crystalline compound fibres

Case	$(\sigma_x^{(1)})_{x=0}$	$(\sigma_x^{(2)})_{x=0}$	$(\sigma_x^{(1)})_{x=1}$	$(\sigma_x^{(2)})_{x=1}$
1	416	647	63,130	63,130
2	373	579	5271	109,884
3	481	748	135,074	7799
4	530	824	77,769	77,769
5	333	518	52,528	52,528
6	317	493	50,439	50,439
7	868	1351	121,448	121,448
8	113	175	24,285	24,285
9	652	1014	93,491	93,491
10	387	447	93,955	9441
11	438	2431	27,901	278,769

Table 3
Nondimensional axial stresses on the core and the sheath for amorphous compound fibres

Case	$(\sigma_x^{(1)})_{x=0}$	$(\sigma_x^{(2)})_{x=0}$	$(\sigma_x^{(1)})_{x=1}$	$(\sigma_x^{(2)})_{x=1}$
1	173	173	27,241	27,241
2	154	154	2645	47,875
3	198	198	55,770	3594
4	216	216	31,498	31,498
5	142	142	24,092	24,092
6	130	130	22,847	22,847
7	354	354	45,274	45,274
8	45	45	14,431	14,431
9	270	270	36,952	36,952
10	167	17	34,675	3467
11	182	1815	19,951	199,511

compound fibres are presented. Although not shown here, the axial stresses on amorphous fibres exhibited similar trends to those shown in Figs. 3, 5, 7, 9 and 11, but are much smaller (by about a factor of, at least, two) than those on liquid crystalline fibres due to the effects of the crystallization on the effective dynamic viscosities of both the core and the sheath (cf. Eqs. (11) and (12)).

4. Discussion and conclusions

A one-dimensional model for slender, Newtonian, liquid crystalline bicomponent or compound fibres has been derived by means of asymptotic methods based on the slenderness ratio as perturbation parameter, from the axisymmetric form of the mass, linear momentum and energy equations for Newtonian fluids. Molecular orientation and crystallization have been included in the resulting one-dimensional model through two equations for the degrees of orientation and crystallization, and additive and multiplicative, respectively, factors in the elongational viscosity law. In addition, the model presented here, accounts for the nonlinear dependence of the dynamic viscosity of the inner and outer fluids on the temperature by means of an Arrhenius expression. The resulting model includes the effects of gravitation, surface tension, axial conduction, heat losses, thermal inertia, molecular orientation and crystallization, but does not account for latent heat effects due to crystallization/solidification, drag on the fibre and the radial variations of the temperature, molecular orientation and crystallization.

It has been shown that the smallness of the slenderness ratio and the Biot number implies that the leading-order temperature is only a function of the axial distance along the fibre, and this places some limitations on the applicability of the model presented here for bicomponent fibres, because it does not provide any information about radial variations of temperature at leading-order and on the implications of these variations on the fibre microstructure. A hybrid two-dimensional model that employs two-dimensional equations for the temperature and the degrees of orientation and crystallization and the one-dimensional equations for the fibre's geometry and axial velocity component derived in this paper, has been suggested to remove some of the limitations discussed above.

Despite these limitations, the one-dimensional model has been applied to study the effects of the activation energy and pre-exponential factor of the elongational dynamic viscosity, heat capacity, thermal conductivity and heat transfer losses on the compound, liquid crystalline fibre's shape, cooling, orientation and crystallization, and it has been shown that the activation energy of the dynamic viscosity plays a paramount role in determining the fibre's shape and the distribution of axial stresses along the fibre. If the activation energy of the core is higher than that of the sheath, it has been shown that the axial stresses on the core are monotonic functions of the axial distance along the fibre, whereas those on the sheath may first increase and then decrease.

It has been shown that the axial strain rate and the degree of molecular orientation increase as the activation energy of the dynamic viscosity of the core, the heat transfer losses, the thermal conductivity ratio and the pre-exponential factors ratio are increased, whereas they decrease as the thermal Péclet number is increased. It has also been shown that the degree of orientation increases until it reaches a value almost equal to one.

For the cases considered in this study, the ultimate degree of crystallization is not achieved along the fibre, and the steepness of the initial crystallization is a strong function of the heat transfer losses and heat conductivity ratio.

Acknowledgements

The research reported in this chapter was supported by Project BFM2001-1902 from the Ministerio de Ciencia y Tecnología and Project FIS2005-03191 from the Ministerio de Educación y Ciencia of Spain and fondos FEDER. The author is grateful to the referees for their comments on the original manuscript.

References

[1] Khan MZS, Simpson G, Gellert EP. Resistance of glass-fibre reinforced polymer composites to increasing compressive strain rates and loading rates. Composites Part A 2000;31:57–67.
[2] Huang J, Baird DG, Loos AC, Rangarajan P, Powell A. Filament winding of bicomponent fibers consisting of polypropelene and a liquid crystalline polymer. Composites Part A 2001;32:1013–20.

[3] Zubia J, Arrue J. Plastic optical fibers: an introduction to their technological processes. Opt Fiber Technol 2001;7:101–40.
[4] Pearson JRA. Mechanics of polymer processing. New York: Elsevier Applied Science Publishers; 1985.
[5] Ziabicki A. Fundamentals of fibre formation. New York: Wiley; 1976.
[6] Ziabicki A, Jarecki A, Wasiak A. Dynamic modelling of melt spinning. Comput Theor Polym Sci 1998;8:143–57.
[7] Park C-W. Extensional flow of a two-phase fiber. AIChE J 1990;36: 197–206.
[8] Lee W-S, Park C-W. Stability of a bicomponent fiber flow. ASME J Appl Mech 1995;62:511–6.
[9] Ji C-C, Yang J-C. Mechanics of steady flow in coextrusion fiber spinning. Polym Eng Sci 1996;36:1399–409.
[10] Ji C-C, Yang J-C, Lee W-S. Stability of Newtonian coextrusion fiber spinning. Polym Eng Sci 1996;36:2685–93.
[11] Naboulsi SK, Bechtel SE. Bicomponent Newtonian fibers. Phys Fluids 1999;11:807–20.
[12] Ramos JI. Asymptotic analysis of compound liquid jets at low Reynolds numbers. Appl Math Comput 1999;100:223–40.
[13] Ramos JI. Compound liquid jets at low Reynolds numbers. Polymer 2002; 43:2889–96.
[14] Kikutani K, Radhakrishnan J, Arikawa S, Takaku A, Okui N, Jin X, et al. High-speed melt spinning of bicomponent fibers: mechanism of fiber structure development in poly(ethylene terephthalate)/polypropylene system. J Appl Polym Sci 1996;62:1913–24.
[15] Landau LD, Lifshitz EM. Statistical physics. Part 1. Course of theoretical physics. vol. 5. New York: Pergamon Press; 1980.
[16] Landau LD, Lifshitz EM. Statistical physics. Part 2. Course of theoretical physics. vol. 9. New York: Pergamon Press; 1980.
[17] Avrami M. Kinetics of phase change. I. General theory. J Chem Phys 1939;7:1103–12.
[18] Avrami M. Kinetics of phase change. II. Transformation-time relations for random distribution of nuclei. J Chem Phys 1940;8:212–24.
[19] Avrami M. Kinetics of phase change. I. Granulation, phase change, and microstructure. J Chem Phys 1941;9:177–84.
[20] Kolmogorov AN. On the statistical theory of the crystallization of metals. Bull Acad Sci USSR, Mathematical Series 1937;1:355–9.
[21] Eder G, Janeschitz-Kriegl H, Liedaues S. Crystallization processes in quiescent and moving polymer melts under heat transfer conditions. Prog Polym Sci 1990;15:629–714.
[22] Eder G. Fundamentals of structure formation in crystallizing polymers. In: Hatada K, Kitayama T, Vogl O, editors. Macromolecular design of polymerica materials. New York: Marcel Dekker; 1997. p. 761–82.
[23] Burger M, Capasso V, Eder G. Modelling of polymer crystallization in temperature fields. ZAMM, Z Angew Math Mech 2002;82:51–63.
[24] Capasso V, editor. Mathematical modelling for polymer processing. New York: Springer; 2003.
[25] Flory PJ. Thermodynamics of crystallization in high polymers I. Crystallization induced by stretching. J Chem Phys 1947;15:397–408.
[26] Rao IJ, Rajagopal RK. A thermodynamic framework for the study of crystallization in polymers. ZAMP, Z Angew Math Phys 2002;53: 365–406.
[27] Forest MG, Zhou H, Wang Q. Thermotropic liquid crystalline polymer fibers. SIAM J Appl Math 2000;60:1177–204.
[28] Doufas AK, McHugh AJ, Miller C. Simulation of melt-spinning including flow-induced crystallization. Part I. Model development and predictions. J Non-Newtonian Fluid Mech 2000;92:27–66.
[29] McHugh AJ, Doufas AK. Modeling flow-induced crystallization in fiber spinning. Composites Part A 2001;32:1059–66.
[30] Ziabicki A, Kawai H, editors. High speed fiber spinning. New York: Wiley; 1985.